© APR 2024 | IRE Journals | Volume 7 Issue 10 | ISSN: 2456-8880
DOI: https://doi.org/10.64388/IREV7I10-1722649

Failure Modes and Fracture-Path Reproducibility in 2D Honeycomb and Diamond Sandwich Architected Cores Under Quasi-Static Loading

BAMIDELE FADAYOMI
Department of Mechanical Engineering, Texas A&M University

Abstract- Architected sandwich cores are widely adopted for their stiffness-to-weight efficiency, yet the literature remains weighted toward stiffness and energy-absorption metrics, with comparatively little systematic data on how such cores actually fracture. This study reports a controlled experimental investigation of failure modes, load-response classification, and fracture-path reproducibility in two-dimensional honeycomb and diamond sandwich cores under quasi-static loading. Eight core configurations were examined: honeycomb at unit-cell angles of 15°, 30° and 45°, diamond at 45°, 90° and 120°, and a functionally graded variant of each topology in which vertical cell height was graded through the core thickness. All specimens were additively manufactured from a UV-cured brittle photopolymer resin, deliberately selected so that fracture rather than plastic collapse would govern, and tested in five replicates per configuration under three-point bending and uniform quasi-static compression. Full-field deformation was recorded by two-dimensional digital image correlation. Core shear governed failure in every honeycomb configuration under both loading modes, whereas the diamond topology exhibited a mode transition with cell angle: buckling dominated at 45° and 90°, while the 120° and functionally graded configurations deformed in a bending-dominated manner with minimal fracture. Load responses conformed to Type II behaviour for the honeycomb and lower-angle diamond cores, with the 15° honeycomb exhibiting a partial Type II response, and to Type I behaviour for the 120° and functionally graded diamond cores. Fracture paths were reproducible in a well-defined subset of configurations, recurring as 180° straight and 120° oblique propagation lines, while the remaining configurations showed no repeatable path. This division is attributed to the interaction between loading-nose position and core strut placement in specimens without enforced core symmetry. The functionally graded cores concentrated deformation within targeted compliant regions while leaving stiffer regions intact, demonstrating spatially programmable failure. The resulting failure-mode map and reproducibility classification provide a quantitative reference dataset for validating numerical models of architected core fracture.

Keywords: architected materials; sandwich structures; honeycomb; diamond lattice; failure modes; fracture reproducibility; functionally graded lattices; digital image correlation; additive manufacturing

I. INTRODUCTION

Architected materials derive their mechanical performance from the deliberate geometric arrangement of a constituent material and of the void space between its members, rather than from the constituent alone [1,2]. Because the governing length scale is geometric rather than microstructural, properties such as stiffness, strength and energy absorption can be specified through topology, which has made architected cores attractive in aerospace, naval, automotive and protective structural applications where mass efficiency is at a premium [3,4]. Two-dimensional prismatic cores, in which a planar unit cell is extruded through the panel thickness, remain the most widely deployed subclass because they are geometrically simple, straightforward to manufacture and well characterised in the stiffness regime.

The mechanical response of lattice cores is conventionally organised around nodal connectivity. The Maxwell stability criterion distinguishes stretching-dominated architectures, which carry load primarily through axial strut forces and exhibit high initial stiffness followed by abrupt post-yield softening, from bending-dominated architectures, which deform through strut flexure and exhibit lower stiffness but extended, more stable collapse plateaux [5,6]. This framework predicts stiffness and collapse strength effectively, and it underpins much of the sandwich-core design literature [7,8]. It is considerably less informative, however, about fracture: it does not predict where a crack initiates within a core, which path that crack follows through the cell array, or whether that path recurs from specimen to specimen.

This gap matters for two reasons. First, in safety-critical use the location and progression of fracture, not merely the peak load, determine residual load-carrying capacity after damage. Second, numerical models of architected failure require experimental data of a specific kind for validation. Comparing a simulated peak load against a measured peak load is a weak test, since many combinations of constitutive and contact assumptions reproduce a single scalar. A far more discriminating test is whether a model reproduces the observed failure mode, the spatial fracture path and the strain field immediately preceding failure. Datasets reporting these quantities systematically, with replication sufficient to establish which observations are reproducible, remain scarce.

Prior experimental work on additively manufactured sandwich cores has established baseline flexural and compressive performance for a range of topologies [13,14], demonstrated the energy-absorption advantages of graded lattices over uniform ones [11,15], and characterised failure mechanisms in meta-sandwich configurations [10]. Studies of tunable printed cores have shown that spatial variation of core geometry can redistribute compliance within a panel [12]. What has received less attention is the reproducibility of fracture itself, treated as a measurable outcome: whether a given architecture fails the same way twice, and what design features determine whether it does.

The present study addresses that question directly. A single constituent material and a single manufacturing route were held fixed while unit-cell angle and grading were varied parametrically across two topologies, and five replicates of every configuration were tested under two quasi-static loading modes. A brittle UV-cured photopolymer was selected deliberately: in a ductile constituent, plastic hinging obscures crack initiation, whereas brittle fracture renders the failure path directly observable and photographically recoverable. The study is organised around three questions:

(i) Which failure mode governs each topology and angular configuration under local (three-point bending) and uniform (quasi-static compression) loading?

(ii) Which aspects of the failure process are reproducible across nominally identical specimens, and which are not?

(iii) How does micro-architecture, including functional grading, govern the fracture path and the spatial distribution of damage?

Low-velocity impact response of the same core configurations is treated separately in a companion study [16]; the present paper is confined to quasi-static behaviour.

II. MATERIALS AND METHODS

2.1 Core architectures and parametric variation

Two planar core topologies were investigated. The honeycomb core comprises tessellated hexagonal unit cells in an in-plane orientation; the diamond core is a reoriented square lattice. Within each topology, a single characteristic unit-cell angle, denoted θ, was varied parametrically while wall thickness and overall core envelope were held constant (Figure 1). Honeycomb cores were produced at θ = 15°, 30° and 45°; diamond cores at θ = 45°, 90° and 120°. The angular ranges differ because the two topologies become geometrically degenerate at different angles.

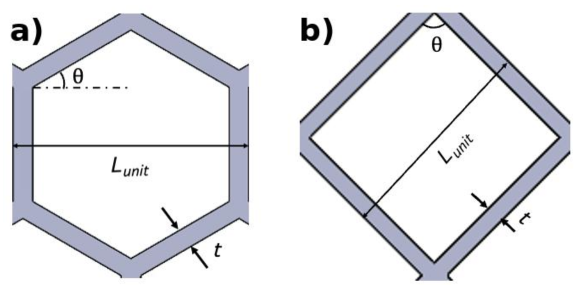

Figure 1. Unit-cell definitions for a) the honeycomb and b) the diamond topology, showing the controlled angle θ, unit-cell length L and wall thickness t.

A functionally graded variant of each topology was additionally produced. Grading was applied to vertical cell height through the core thickness according to a prescribed growth function, so that cell height increases progressively from one face toward the other. This produces a monotonic through-thickness compliance gradient while leaving the in-plane topology unchanged, isolating the effect of grading from that of cell shape. Eight configurations resulted:

four honeycomb (15°, 30°, 45°, graded) and four diamond (45°, 90°, 120°, graded).

2.2 Specimen geometry

Two specimen geometries were used to suit the two loading modes (Figure 2). Sandwich beams measuring 135 x 25 x 48 mm were used for three-point bending, and sandwich panels measuring 80 x 80 x 48 mm for uniform compression. In both geometries the face plate thickness was fixed at 4 mm and the core thickness at 40 mm, so that the face-to-core ratio was identical across all configurations and loading modes. All specimens except the functionally graded honeycomb were modelled in SOLIDWORKS 2021; the graded honeycomb geometry was constructed in Blender v3.3.1, which permitted direct implementation of the grading function. Nominal CAD dimensions and densities were used as the reference for all comparative analysis, since small dimensional deviations are introduced by the cure and wash stages of the manufacturing route.

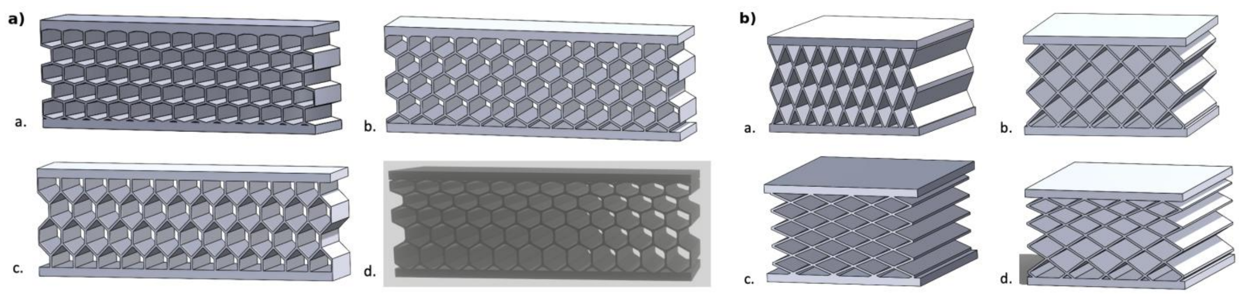

Figure 2. Specimen families: a) honeycomb sandwich beams at 15°, 30°, 45° and functionally graded; b) diamond sandwich panels at 45°, 90°, 120° and functionally graded.

2.3 Material and manufacturing

All specimens were manufactured from ANYCUBIC Basic UV-curable photopolymer resin, comprising approximately 60 percent epoxy resins, 35 percent (1-methyl-1,2-ethanediyl)bis[oxy(methyl-2,1-ethanediyl)] diacrylate and 5 percent hydroxycyclohexyl phenyl ketone. A brittle post-cure constituent was selected deliberately so that specimen failure would occur by fracture and be directly observable, rather than by distributed plastic hinging.

Specimens were printed on an ANYCUBIC Photon Mono X LCD resin printer, washed in 99 percent isopropyl alcohol for 5 to 10 minutes, and post-cured for 2 minutes in an ANYCUBIC UV curing station. Parts were oriented at 45° during printing to reduce the peel area against the vat film and limit warping. Across this study and the companion impact study [16] a total of 120 specimens were fabricated, comprising 5 replicates for each of 8 configurations under each of 3 loading conditions; the 80 specimens tested under the two quasi-static modes are reported here.

2.4 Bulk material characterisation

Constituent properties were characterised prior to structural testing so that core response could be separated from constituent response. Flexural properties were obtained per ASTM C1161-13 using prism samples of 140 x 6 x 8 mm over a 100 mm span at 5 mm/min. Compressive properties followed ASTM D695-15 using 12.7 x 12.7 x 25.4 mm samples at 2 mm/min, and tensile properties followed ASTM D638-14 using dogbone specimens at 5 mm/min. Five specimens were tested per configuration on a Newton universal testing machine (UTM). Results are summarised in Table 1. The compressive stress-strain response was consistent across replicates, with standard deviations within 12 percent of the corresponding means, and exhibited abrupt brittle failure at peak stress with negligible post-peak ductility, confirming the intended constituent behaviour.

Table 1. Measured mechanical properties of the UV-cured ANYCUBIC photopolymer constituent (mean ± standard deviation, five replicates).

Mechanical property	Value	Test standard
Tensile strength (MPa)	22.192 ± 2.317	ASTM D638-14
Tensile modulus (GPa)	0.528 ± 0.040	ASTM D638-14
Flexural strength (MPa)	25.193 ± 2.240	ASTM C1161-13
Flexural stiffness (GPa)	0.608 ± 0.074	ASTM C1161-13
Compressive strength (MPa)	55.785 ± 6.474	ASTM D695-15
Compressive stiffness (GPa)	1.048 ± 0.069	ASTM D695-15

2.5 Quasi-static test procedures

All tests were conducted at room temperature on a Newton UTM under crosshead displacement control. In three-point bending, sandwich beams were supported over a 100 mm span and loaded centrally at 5 mm/min to a total deflection of 24 mm, corresponding to 50 percent of the beam depth. In uniform compression, sandwich panels were compressed between two 116 mm diameter circular steel platens at 2 mm/min to 20 mm, corresponding to 50 percent of the core depth. Post-test photographs of the compression specimens were captured at 10 mm displacement, that is, at 25 percent core deformation, so that fracture paths could be documented before densification obscured them. Peak load was taken as the maximum recorded force, and absorbed energy as the area under the load-displacement curve to the prescribed displacement limit.

2.6 Digital image correlation

Selected specimens were prepared for two-dimensional digital image correlation (DIC) to obtain full-field displacement and strain data on the front-facing core plane. Specimens were coated with matte white paint applied by roller, and a dense black speckle pattern was applied using a toothbrush. Images were captured with a Sony A7IV camera fitted with a 35 mm lens, and correlation was performed in DICe, the open-source Digital Image Correlation engine developed by Sandia National Laboratories. Reported strain fields are global fields resolved on the imaged plane and are not referred to individual strut axes; they are therefore used here to identify the dominant deformation mechanism and its spatial distribution, not to extract local strut-level strain magnitudes. Correlation is additionally unreliable at large displacements, and not all specimens yielded usable correlation results; DIC observations are accordingly reported for the subset of specimens in which correlation was successful.

III. RESULTS

3.1 Three-point bending

Under local loading the two topologies separated sharply in load-carrying capacity. Within the honeycomb family, peak load decreased as θ increased from 15° to 45°, from 413.46 ± 31.22 N to 315.24 ± 5.61 N, while absorbed energy remained comparatively flat, ranging from 3.521 ± 0.377 J to 5.019 ± 0.423 J. The functionally graded honeycomb recovered much of the load capacity of the 15° configuration at 399.90 ± 34.07 N. That peak load varied by roughly 24 percent across the honeycomb family while absorbed energy varied without a consistent trend indicates that in this topology the unit-cell angle principally governs strength rather than total dissipation capacity. The load-displacement response of the 15° honeycomb beams and the characteristic Type II trend extracted from it are shown in Figure 3.

© APR 2024 | IRE Journals | Volume 7 Issue 10 | ISSN: 2456-8880
DOI: https://doi.org/10.64388/IREV7I10-1722649

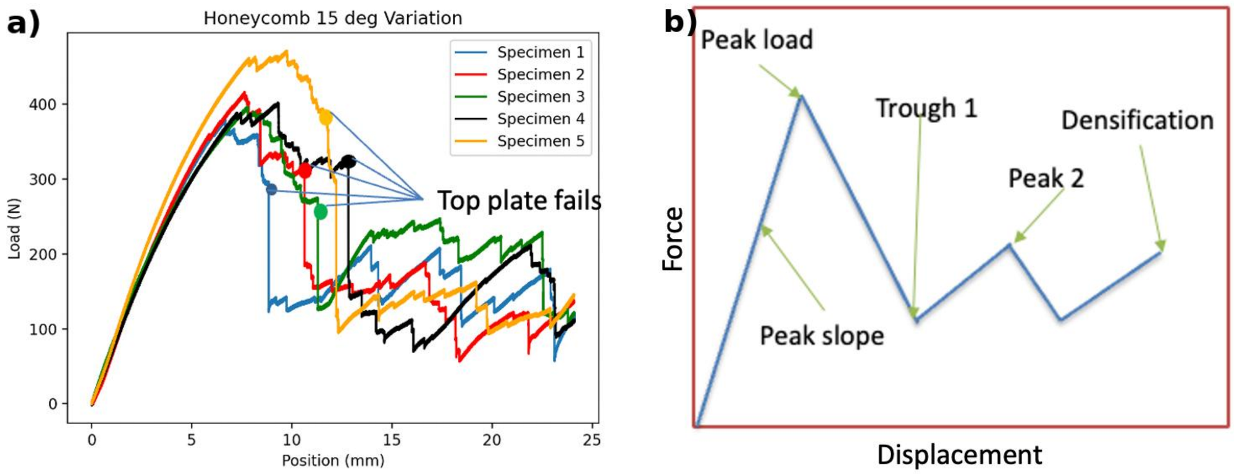

Figure 3. a) Load-displacement response of the five 15° honeycomb sandwich beams under three-point bending; b) characteristic Type II response trend, showing peak load, post-peak trough, secondary peak and densification.

The diamond family showed markedly greater angular sensitivity. The 45° configuration reached 1126.47 ± 263.87 N, approximately 2.7 times the strongest honeycomb configuration under the same loading, and absorbed 7.964 ± 2.367 J. Increasing θ to 90° reduced peak load to 685.05 ± 132.35 N, and at 120° the peak load fell to 339.01 ± 24.90 N, a reduction of about 70 percent relative to the 45° configuration. The graded diamond core recorded the lowest peak load of any configuration at 253.21 ± 75.73 N while still absorbing 4.922 ± 0.404 J. Full results are given in Table 2.

Table 2. Peak load, absorbed energy and dominant failure mode under three-point bending (mean ± standard deviation, five replicates per configuration).

Configuration	Peak load (N)	Absorbed energy (J)	Dominant mode
Honeycomb 15°	413.46 ± 31.22	5.019 ± 0.423	Core shear
Honeycomb 30°	324.75 ± 24.29	3.521 ± 0.377	Core shear
Honeycomb 45°	315.24 ± 5.61	3.651 ± 0.248	Core shear
Honeycomb graded	399.90 ± 34.07	4.979 ± 0.860	Core shear
Diamond 45°	1126.47 ± 263.87	7.964 ± 2.367	Buckling
Diamond 90°	685.05 ± 132.35	6.364 ± 2.388	Buckling
Diamond 120°	339.01 ± 24.90	5.328 ± 0.202	Bending
Diamond graded	253.21 ± 75.73	4.922 ± 0.404	Bending

3.2 Quasi-static compression

Under uniform compression every configuration sustained substantially higher loads than under local bending, confirming that distributed loading engages a greater proportion of the core volume before failure initiates. Honeycomb peak loads increased monotonically with θ, from 1713.70 ± 446.45 N at 15° to 2283.27 ± 52.34 N at 45°, reversing the trend observed in bending. The functionally graded honeycomb achieved both the highest peak load and the highest absorbed energy of the honeycomb family, at 2800.81 ± 82.41 N and 24.015 ± 0.913 J.

The 45° diamond configuration recorded the highest values measured anywhere in this study, at 8455.89 ± 138.33 N and 54.637 ± 1.151 J, exceeding the strongest honeycomb configuration by a factor of approximately three; its load-displacement response and post-failure state are shown in Figure 4. Peak load then fell steeply with increasing θ, to 2406.92 ± 164.84 N at 90° and 408.19 ± 82.57 N at 120°. The graded diamond core recorded 509.28 ± 70.65 N and 10.036 ± 0.724 J. The dispersion of the 45° diamond and 45° honeycomb results was notably low, with standard deviations of 1.6 percent and 2.3 percent of the mean respectively, indicating highly repeatable collapse initiation in those configurations. Results are summarised in Table 3.

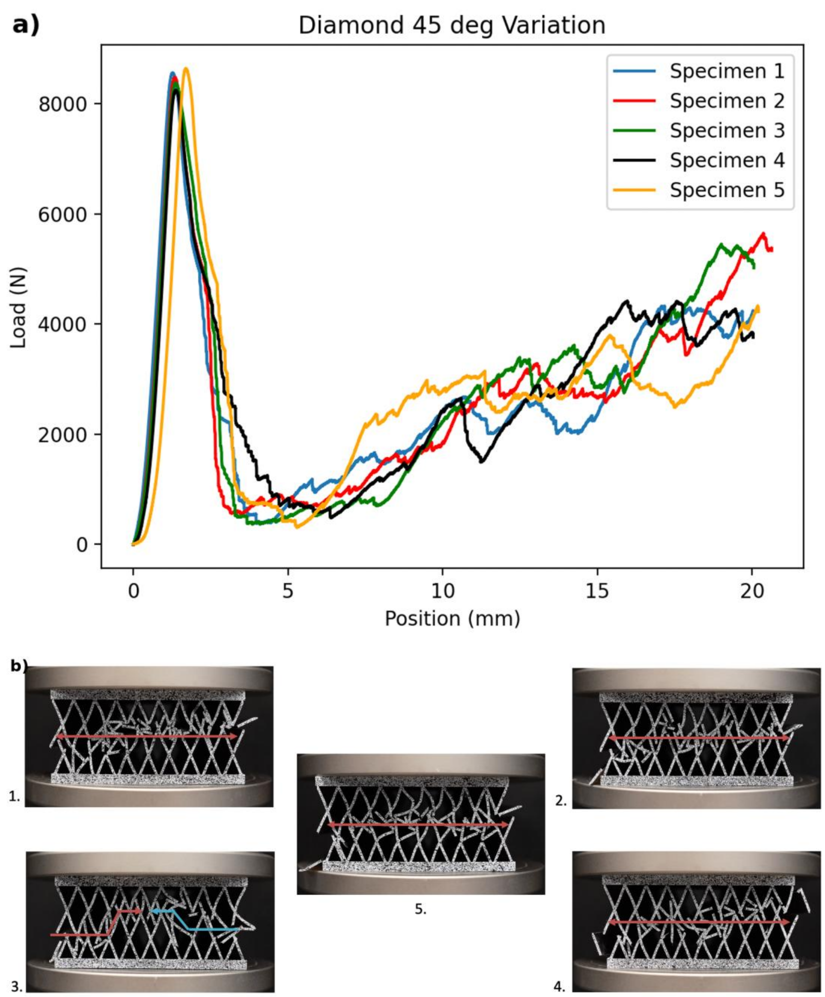

Figure 4. 45° diamond sandwich panels under quasi-static compression: a) load-displacement response of the five replicates; b) post-failure images at 25 percent core deformation, showing the reproducible 180° fracture path through the middle row.

© APR 2024 | IRE Journals | Volume 7 Issue 10 | ISSN: 2456-8880
DOI: https://doi.org/10.64388/IREV7I10-1722649

Table 3. Peak load, absorbed energy and load-response classification under quasi-static compression (mean ± standard deviation, five replicates per configuration).

Configuration	Peak load (N)	Absorbed energy (J)	Response type
Honeycomb 15°	1713.70 ± 446.45	15.791 ± 3.720	Partial Type II
Honeycomb 30°	1778.61 ± 110.21	13.775 ± 1.074	Type II
Honeycomb 45°	2283.27 ± 52.34	14.323 ± 1.455	Type II
Honeycomb graded	2800.81 ± 82.41	24.015 ± 0.913	Type II
Diamond 45°	8455.89 ± 138.33	54.637 ± 1.151	Type II
Diamond 90°	2406.92 ± 164.84	17.498 ± 1.469	Type II
Diamond 120°	408.19 ± 82.57	8.746 ± 0.273	Type I
Diamond graded	509.28 ± 70.65	10.036 ± 0.724	Type I

3.3 Failure modes

Core shear governed all four honeycomb configurations under both loading modes. The near-horizontal cell walls sheared preferentially relative to the more steeply inclined walls, producing a characteristic step-like collapse that advanced row by row. Buckling was present as a secondary mechanism and was more pronounced under compression than under bending.

The diamond topology exhibited a mode transition governed by θ. At 45° and 90°, the steep strut inclination promoted axial loading of the struts and failure occurred by buckling; in bending, face-sheet failure preceded significant core damage in the 45° configuration. At 120° and in the graded configuration, the obtuse cell angle reduced effective nodal constraint, shifting the architecture toward the under-constrained, bending-dominated regime consistent with the transition anticipated by the Maxwell criterion [5,6]. These configurations deformed extensively by strut flexure with little or no fracture, and the corresponding load response changed character accordingly, as reported in Section 3.4.

3.4 Load-response classification

Load responses were classified against the Type I and Type II framework of Calladine and English [9]. Type II behaviour, characterised by a sharp initial peak followed by progressive softening as damage accumulates, was observed in all honeycomb configurations and in the 45° and 90° diamond configurations. The 15° honeycomb was classified as partial Type II, because subsequent load peaks equalled or exceeded the initial peak in all five replicates, reflecting sequential engagement of successive cell rows rather than a single dominant collapse event.

Type I behaviour, characterised by a steadily rising load over large strain without a distinct initial peak, was observed in the 120° and functionally graded diamond configurations. This classification aligns with the failure-mode observations: the configurations that deform by bending without fracture sustain progressively increasing load as struts rotate and stiffen, whereas configurations that fracture exhibit load drops at each fracture event.

3.5 Fracture-path reproducibility

Fracture paths divided the eight configurations into two clearly separated groups. Reproducible paths, recurring in the same location and orientation across all five replicates, were observed in the 15° honeycomb, the 30° honeycomb under bending, the functionally graded honeycomb, and the 45° and 90° diamond configurations under compression. In these cases the paths took one of two forms: a 180° straight line propagating through a single cell row, or a 120° oblique line propagating diagonally across rows. The five 15° honeycomb beams in Figure 5 illustrate the recurrence of the path across replicates.

© APR 2024 | IRE Journals | Volume 7 Issue 10 | ISSN: 2456-8880
DOI: https://doi.org/10.64388/IREV7I10-1722649

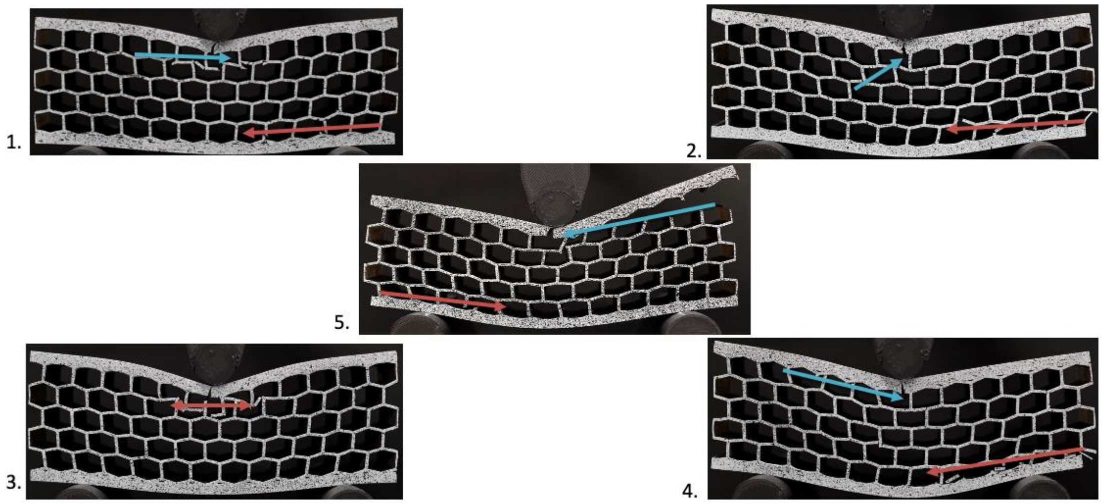

Figure 5. Post-failure images of the five 15° honeycomb sandwich beams after three-point bending, with the recurring fracture paths marked, illustrating path reproducibility across replicates.

Specifically, the 15° honeycomb fractured along opposing straight 180° paths on the top and bottom rows under bending, and by a step-like ascending process from the bottom row under compression. The 30° honeycomb showed opposing 120° and 180° lines on the bottom and top rows under bending. The functionally graded honeycomb produced a 120° path initiating at the bottom row under both loading modes. Under compression, the 45° diamond fractured along a straight 180° path through the middle row, with the entire row collapsing by strut buckling (Figure 4b), while the 90° diamond showed a primary 120° path from the top row and a secondary 180° path through the bottom row.

No reproducible path was observed in the 45° honeycomb under either mode, the 30° honeycomb under compression, or the 45° and 90° diamond configurations under bending. The 120° and graded diamond configurations sustained too little fracture for a path to be defined; instead they showed localised large deformation, concentrated in the central region of the first three rows under bending and in the third row under compression. Table 4 summarises the classification.

Table 4. Fracture-path reproducibility across five replicates per configuration and loading mode.

Configuration	Bending	Compression	Characteristic path
Honeycomb 15°	Reproducible	Reproducible	180° opposing / step-like
Honeycomb 30°	Reproducible	Not reproducible	120° and 180° opposing
Honeycomb 45°	Not reproducible	Not reproducible	—
Honeycomb graded	Reproducible	Reproducible	120° from bottom row
Diamond 45°	Not reproducible	Reproducible	180° through middle row

© APR 2024 | IRE Journals | Volume 7 Issue 10 | ISSN: 2456-8880
DOI: https://doi.org/10.64388/IREV7I10-1722649

Configuration	Bending	Compression	Characteristic path
Diamond 90°	Not reproducible	Reproducible	120° top, 180° bottom
Diamond 120°	Minimal fracture	Minimal fracture	Localised deformation
Diamond graded	Minimal fracture	Minimal fracture	Localised deformation

3.6 Full-field deformation

DIC analysis corroborated the visually identified failure modes. In the honeycomb configurations for which correlation was successful, shear strain was the dominant field component immediately preceding core failure, confirming core shear as the governing mechanism rather than inferring it from post-test appearance alone. In the 45° diamond configuration under bending, lateral strain dominated, consistent with the onset of the lateral strut deflection characteristic of buckling.

Vertical displacement maps additionally quantified the through-core displacement gradient. In the functionally graded honeycomb under bending (Figure 6), vertical displacement decayed continuously from a maximum of approximately 4.41 mm at the loading-nose contact point toward effectively zero at the supports, providing a spatially resolved field suitable for direct comparison with numerical predictions.

Figure 6. DIC vertical (y-axis) displacement map (mm) for a functionally graded honeycomb specimen under three-point bending, showing the gradient from the loading-nose contact point to the supports.

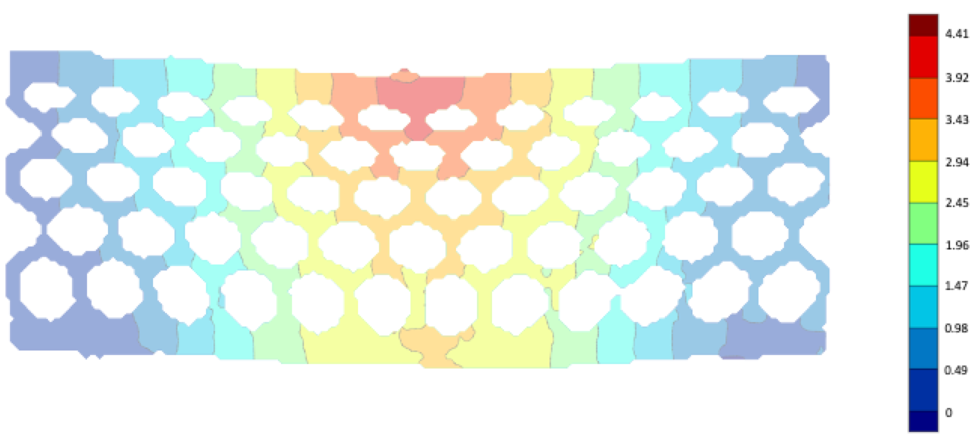

IV. DISCUSSION

4.1 Angular sensitivity differs fundamentally between topologies

The two topologies respond to angular variation in qualitatively different ways, and the difference is mechanistic rather than merely quantitative. In the honeycomb cores, varying θ from 15° to 45° changed peak load without changing the governing failure mode: core shear dominated throughout. Angle therefore acts principally as a strength-scaling parameter in this topology, which is consistent with absorbed energy remaining comparatively flat across the honeycomb family under bending.

In the diamond cores, varying θ changed the failure mechanism itself. The progression from buckling at 45° and 90° to bending-dominated deformation at 120° corresponds to a reduction in effective nodal constraint as the cell angle becomes obtuse, moving the architecture across the stretching-to-bending boundary described by the Maxwell criterion [5,6]. This is why the diamond family spans a factor of approximately twenty in compressive peak load, from 8455.89 N at 45° to 408.19 N at 120°, while the honeycomb family spans less than a factor of two. For design purposes the implication is that the diamond topology offers a single geometric parameter capable of selecting between a stiffness-optimised and a compliance-optimised structure, whereas the honeycomb topology does not.

4.2 Loading mode redistributes performance

Every configuration sustained its highest load under uniform compression and its lowest under three-point bending. This ordering reflects the volume of core engaged before failure initiates: distributed platen loading recruits the full core cross-section, whereas a central loading nose concentrates stress in the cells immediately beneath it and initiates local failure at a lower global load.

More notable is that the ranking within the honeycomb family inverts between the two modes. Under bending, peak load decreased with increasing θ, with the 15° configuration strongest; under compression, peak load increased with θ, with the 45° configuration strongest among the uniform cores. A configuration optimised against one quasi-static loading mode is therefore not necessarily optimal against the other, and single-mode characterisation is insufficient to rank architectures for service conditions involving both.

4.3 Reproducibility is a design-controllable property

The most consequential finding for numerical validation is that fracture-path reproducibility is not uniform across architectures but divides the configurations into two well-defined groups. The configurations without reproducible paths share a specific geometric characteristic: core symmetry was not enforced during specimen design, so the position of the loading nose relative to the underlying strut arrangement varied between nominally identical specimens. Where the nose bears directly on a node, load transfers into the core differently than where it bears between nodes, and initiation shifts accordingly. Configurations in which the cell size is small relative to the contact region, or in which a graded compliance field predetermines the initiation site, are insensitive to this variation and fracture reproducibly.

This has a direct practical consequence. Reproducibility should be treated as a property that specimen design controls, not as an inherent attribute of a topology. Enforcing core symmetry and fixing the loading-nose position relative to the cell array would be expected to convert several of the non-reproducible configurations into reproducible ones, and this is a necessary control in any test programme intended to generate validation data. The distinction also indicates which of the present configurations are suitable as validation cases: a model should be expected to reproduce the path in the reproducible group, whereas in the non-reproducible group only statistical distributions of initiation site are meaningful.

4.4 Functional grading yields spatially programmable failure

The functionally graded configurations behaved in a way that neither uniform family reproduces. Under both bending and compression, deformation localised in the more compliant, larger-angle regions of the core while the stiffer regions remained largely undamaged. Damage location was therefore set by the grading function rather than by the loading configuration, which is the practical content of the tunability observed here.

This is design-relevant in two ways. It allows damage to be directed away from regions that must retain integrity, for instance load-introduction points or attachment features. It also decouples strength from dissipation: the graded honeycomb achieved both the highest peak load and the highest absorbed energy of its family under compression, at 2800.81 N and 24.015 J, indicating that grading need not be paid for with a reduction in strength. The graded honeycomb also fractured reproducibly under both loading modes, supporting the interpretation in Section 4.3 that a predetermined compliance gradient fixes the initiation site and thereby suppresses specimen-to-specimen variation.

4.5 Limitations

Three limitations bound the interpretation of these results. First, relative density was not held constant across configurations, since the envelope and wall thickness were fixed while cell angle varied. Absolute performance values are therefore not directly comparable between configurations of differing density, and comparisons in this paper are drawn within families and between failure modes rather than as density-normalised rankings. A density-controlled study is required before topologies can be ranked on specific performance.

Second, core symmetry was not enforced, which as discussed above introduced variability in load introduction and is the most probable cause of the non-reproducible fracture paths. Third, the constituent was a brittle photopolymer selected to render fracture observable. The failure-mode map and reproducibility classification reported here should therefore be understood as applying to brittle-constituent architected cores; ductile constituents would be expected to substitute plastic hinging for fracture in at least some of these configurations, and the transition angles may shift accordingly.

V. CONCLUSION

A controlled experimental study of failure in two-dimensional honeycomb and diamond sandwich architected cores under quasi-static loading supports the following conclusions.

1. Core shear governed failure in all honeycomb configurations under both three-point bending and uniform compression. In the diamond topology the governing mode changed with unit-cell angle, from buckling at 45° and 90° to bending-dominated deformation with minimal fracture at 120° and in the graded configuration.

2. Unit-cell angle acts as a strength-scaling parameter in the honeycomb topology but as a mode-selection parameter in the diamond topology, which consequently spans a factor of approximately twenty in compressive peak load, from 8455.89 N at 45° to 408.19 N at 120°.

3. Load responses conformed to Type II behaviour in all honeycomb configurations and in the 45° and 90° diamond configurations, with the 15° honeycomb exhibiting a partial Type II response, and to Type I behaviour in the 120° and functionally graded diamond configurations, consistent with the classification of Calladine and English.

4. Fracture paths were reproducible across five replicates in a well-defined subset of configurations, recurring as 180° straight and 120° oblique propagation lines. Non-reproducible configurations are attributed to unconstrained loading-nose position relative to the strut array in specimens without enforced core symmetry, indicating that fracture reproducibility is controllable through specimen design.

5. Functionally graded cores localised deformation within targeted compliant regions while leaving stiffer regions intact, and did so without sacrificing strength: the graded honeycomb recorded both the highest peak load and the highest absorbed energy of its family under compression.

6. The combined failure-mode map, reproducibility classification and full-field displacement data constitute a validation-grade dataset against which numerical models of architected core fracture can be tested on failure mode and spatial path, rather than on peak load alone.

Future work should enforce core symmetry and fix loading-nose position relative to the cell array to test the reproducibility mechanism proposed here, and should introduce relative-density constraints to permit equitable comparison across topologies. Extension of the present dataset to finite element model validation is the subject of ongoing work.

REFERENCES

[1] M. F. Ashby and Y. J. M. Bréchet, "Designing hybrid materials," *Acta Materialia*, vol. 51, no. 19, pp. 5801–5821, 2003. ScienceDirect

[2] J. R. Greer and V. S. Deshpande, "Three-dimensional architected materials and structures: Design, fabrication, and mechanical behavior," *MRS Bulletin*, vol. 44, no. 10, pp. 750–757, 2019. Cambridge

[3] L. J. Gibson and M. F. Ashby, *Cellular Solids: Structure and Properties*, 2nd ed. Cambridge: Cambridge University Press, 1997.

[4] M. F. Ashby, "The properties of foams and lattices," *Philosophical Transactions of the*

Royal Society A, vol. 364, no. 1838, pp. 15–30, 2006. Royal Society

[5] S. Deshpande, M. F. Ashby, and N. A. Fleck, "Foam topology: bending versus stretching dominated architectures," *Acta Materialia*, vol. 49, no. 6, pp. 1035–1040, 2001. ScienceDirect

[6] J. C. Maxwell, "On reciprocal figures and diagrams of forces," *Philosophical Magazine*, vol. 27, no. 182, pp. 250–261, 1864.

[7] H. N. G. Wadley, N. A. Fleck, and A. G. Evans, "Fabrication and structural performance of periodic cellular metal sandwich structures," *Composites Science and Technology*, vol. 63, no. 16, pp. 2331–2343, 2003. ScienceDirect

[8] N. A. Fleck, V. S. Deshpande, and M. F. Ashby, "Micro-architectured materials: past, present and future," *Proceedings of the Royal Society A*, vol. 466, no. 2121, pp. 2495–2516, 2010. Royal Society

[9] C. R. Calladine and R. W. English, "Strain-rate and inertia effects in the collapse of two types of energy-absorbing structure," *International Journal of Mechanical Sciences*, vol. 26, no. 11–12, pp. 689–701, 1984. ScienceDirect

[10] H. Yazdani Sarvestani, A. H. Akbarzadeh, A. Mirbolghasemi, and K. Hermenean, "3D printed meta-sandwich structures: Failure mechanism, energy absorption and multi-hit capability," *Materials & Design*, vol. 160, pp. 179–193, 2018. ScienceDirect

[11] H. Niknam and A. H. Akbarzadeh, "Graded lattice structures: Simultaneous enhancement in stiffness and energy absorption," *Materials & Design*, vol. 196, p. 109129, 2020. ScienceDirect

[12] T. Li and L. Wang, "Bending behavior of sandwich composite structures with tunable 3D-printed core materials," *Composite Structures*, vol. 175, pp. 46–57, 2017. ScienceDirect

[13] S. M. Zaharia, L. A. Enescu, and M. A. Pop, "Mechanical Performances of Lightweight Sandwich Structures Produced by Material Extrusion-Based Additive Manufacturing," *Polymers*, vol. 12, no. 8, 2020. MDPI

[14] N. Kladovasilakis et al., "Experimental and Computational Investigation of Lattice Sandwich Structures Constructed by Additive Manufacturing Technologies," *Journal of Manufacturing and Materials Processing*, vol. 5, no. 3, 2021. MDPI

[15] I. Maskery et al., "A mechanical property evaluation of graded density Al-Si10-Mg lattice structures manufactured by selective laser melting," *Materials Science and Engineering A*, vol. 670, pp. 264–274, 2016. ScienceDirect

[16] B. Fadayomi, "Low-Velocity Impact Response and Force Transmission in 2D Architected Sandwich Cores: Effect of Cell Angle and Functional Grading," companion manuscript, submitted concurrently.